crystals

MDPI

Article

Laser Irradiation-Induced Nanoscale Surface Transformations in Strontium Titanate

Ashish Kumar Gupta [1], Siddharth Gupta [2], Soumya Mandal [1] and Ritesh Sachan [1,*]

[1] School of Mechanical and Aerospace Engineering, Oklahoma State University, Stillwater, OK 74078, USA; ashish.gupta10@okstate.edu (A.K.G.); smandal@okstate.edu (S.M.)
[2] Materials Science and Engineering, North Carolina State University, Raleigh, NC 27606, USA; sgupta32@ncsu.edu
* Correspondence: rsachan@okstate.edu

Abstract: We studied the structural transformations and atomic rearrangements in strontium titanate ($SrTiO_3$) via nanosecond pulsed laser irradiation-induced melting and ultrafast quenching. Using scanning transmission electron microscopy, we determine that the laser-irradiated surface in single-crystalline $SrTiO_3$ transforms into an amorphous phase with an interposing disordered crystalline region between amorphous and ordered phases. The formation of disordered phase is attributed to the rapid recrystallization of $SrTiO_3$ from the melt phase constrained by an epitaxial relation with the pristine region, which eases up on the surface, leading to amorphous phase formation. With electron energy-loss spectroscopic analysis, we confirm the transformation of Ti^{+4} to Ti^{+3} due to oxygen vacancy formation as a result of laser irradiation. In the disordered region, the maximum transformation of Ti^{+4} is observed to be 16.2 ± 0.2%, whereas it is observed to be 20.2 ± 0.2% in the amorphous region. Finally, we deduce that the degree of the disorder increases from atomically disordered to amorphous transition in $SrTiO_3$ under laser-irradiation. The signatures of short-range ordering remain similar, leading to a comparable fingerprint of electronic structure. With these results, this study addresses the gap in understanding the atomic and electronic structure modified by pulsed laser irradiation and functionalizing pristine $SrTiO_3$ for electronic, magnetic, and optical applications.

Keywords: pulsed laser irradiation; strontium titanate; high-angle annular dark-field imaging; electron energy-loss spectroscopy; oxygen vacancies

Citation: Gupta, A.K.; Gupta, S.; Mandal, S.; Sachan, R. Laser Irradiation-Induced Nanoscale Surface Transformations in Strontium Titanate. *Crystals* **2022**, *12*, 624. https://doi.org/10.3390/cryst12050624

Academic Editors: Dejun Li and Francisco M. Morales

Received: 9 March 2022
Accepted: 22 April 2022
Published: 27 April 2022

1. Introduction

Laser irradiation in strontium titanate ($SrTiO_3$) results in atomic rearrangement and phase transitions on the surfaces and sub-surfaces via ultrafast melting and recrystallization processes [1–3]. This introduces several non-equilibrium atomic-level defects in materials [4,5]. Its effect on the evaluation of defects [6–8], novel nanostructure [9,10], and phase transformations [11,12] is critical and needs to be studied in detail. Furthermore, these atomic-scale structural modifications are becoming increasingly important in manipulating the functional properties [13–17]. Recently, various studies involving defect engineering in $SrTiO_3$ using laser irradiation approaches have been reported, giving rise to several important properties, such as blue-light emission [18], metastable ferroelectricity [19], and localized conductivity due to the formation of oxygen vacancy defects [20] that are commonly not expected in the stoichiometric composition.

The properties of $SrTiO_3$, a well-known wide-bandgap material, are strongly influenced by non-stoichiometry [21]. The adaptable defect chemistry in $SrTiO_3$ makes it a suitable candidate for electrical [22,23], photonic [24,25], and magnetic applications [26] that can be greatly influenced by increasing the concentration of oxygen vacancies. This results in the distortion of TiO_6 octahedra [27,28] and transformation of Ti^{+4} to Ti^{+3}. This non-stoichiometry in the crystal lattice can be simply modified with the introduction of oxygen vacancies through laser irradiation [2]. The controlled interplay of oxygen vacancies in the crystal lattice is presently utilized in multiple applications, such as tunable microwave devices [29,30], dynamic random-access memory [29], photocatalysis [31,32], potential anodes for solid oxide fast-ion conductors [33,34], and cathode luminescence [18,35]. The availability of multiple oxidation states facilitates bulk transport properties for electronic applications [36]. It is revealed that the transformation of Ti^{+4} to Ti^{+3}, $SrTiO_3$ exhibits n-type semiconducting behavior [34]. This reduction of oxidation states of transition metal ions is effective in creating electronic carriers to pass current, and it is likely to enhance oxide ion conductivity [34].

In this study, we demonstrate a study on atomic rearrangements and localized modifications in electronic structure via pulsed laser irradiated $SrTiO_3$. Laser parameters were first optimized by performing nanoscale heat transfer simulations over $SrTiO_3$. A 2D model was used to estimate the local thermal profile on the surface of $SrTiO_3$ at different laser energy densities by solving the time-dependent heat equations. Then, pristine single crystal $SrTiO_3$ was irradiated using a single pulse of an ArF excimer laser at the optimized energy. To investigate the compositional and structural changes in the surface and subsurface regions in $SrTiO_3$ due to pulsed laser irradiation, atomic-resolution imaging and electron energy-loss spectroscopy (EELS) analysis using a scanning transmission electron microscope were conducted. This study enables a systematic understanding of solid-state chemistry to open new avenues of material design by defect engineering for electronics and energy applications.

2. Materials and Methods

The nanoscale heat transfer simulation of $SrTiO_3$ was performed with a 2D finite element model utilizing the time-dependent heat transfer in solids in COMSOL Multiphysics. Heat transfer mode and transient analysis in the conduction type of heat transfer was considered for thermal modeling. A single pulse of the ArF excimer laser (193 nm wavelength, 25 ns pulse width) was incident on the top surface. In the simulation, the top surface was allowed to conduct heat for unidirectional heat flow, whereas the remaining three side surfaces were considered thermally insulated in the two-dimensional rectangular geometry. The initial temperature or ambient temperature was set at 293 K. Cooling through convection and the surface-to-ambient radiation boundary conditions were applied on the top surface, which initiated the crystallization process even faster. Mesh elements having an extremely fine distribution with a maximum size of 2 nm were chosen for the better accuracy of the intended solutions. The range of time was selected from 0 ns to 100 ns with a step size of 0.01 ns to calculate the thermal profile.

Laser irradiation on commercially purchased single crystalline (100) $SrTiO_3$ (dimensions 10 mm × 10 mm × 1 mm, MTI corporation) was performed using a single pulse of the ArF excimer laser (193 nm wavelength, 20 ns pulse width) with 300 $mJ \cdot cm^{-2}$ energy density as identified through numerical thermal simulations. In this experiment, laser was irradiated with normal incidence on $SrTiO_3$ crystal. Focus ion beam (FIB) (FEI Quanta 3D FEG) with dual electron and ion beams was used for preparing cross-sectional STEM samples. The thin layer of Pt (~2 µm) was deposited on samples using the combination of electron beam 10 pA and Ga ion beam operated at 1 nA to protect the surface from further beam damage that may occur during sample preparation. Initial specimen thinning was performed at 30 kV Ga beam accelerating voltage. To minimize the possibility of Ga implantation and surface damage, a recipe for TEM specimen preparation in FIB was used, consisting of several steps where Ga ion beam energy and current were gradually lowered to 5 kV/10 pA. This was used to clean up the beam-induced surface damage of the FIB lamella. A final low energy ion beam (0.5 kV, 10 pA) was used to clean up the focused ion beam (FIB) surface damage. Atomic-resolution, high-angle annular dark-field (HAADF) imaging was performed in this study using aberration-corrected Nion UltraSTEM200 scanning transmission electron microscopes (STEM) operated at 200 keV. HAADF imaging was conducted with a collection inner semi-angle of 65 mrad and an electron probe current of 28 ± 2 pA in a Nion UltraSTEM 200. While the images were obtained at high collection semi-angles (>65 mrad), we observe considerable strain contrast in the disordered region. Thus, the images will be referred to as annular dark-field (ADF) in the entire study. The EELS data were acquired with a collection angle of 48 mrad. Energy dispersion of 0.1 eV/channel and spatial pixel size of 0.04 nm were utilized to acquire fine structure EELS data over the selected area of interest. To obtain elemental mapping, 0.5 eV/channel energy dispersion and 0.27 nm spatial pixel size were utilized.

3. Results

In this study, thermal simulations are first conducted to identify the laser irradiation parameters to irradiate $SrTiO_3$. A temperature evaluation as a function of time on the surface of $SrTiO_3$ is presented in Figure 1a at laser energy densities ranging from 50 mJ·cm^{-2} to 300 mJ·cm^{-2}. It is determined that a minimum energy density of ~300 mJ·cm^{-2} is sufficient to melt $SrTiO_3$ using ArF nanosecond pulsed laser. Below that, there is no indication of material temperature reaching up to $SrTiO_3$ melting point (2080 °C), thus no solid to liquid transformation occurs. The thermal profile also suggests a rapid melting and cooling of $SrTiO_3$ under laser-solid transient interaction where the maximum temperature increases with increasing laser energy density and rises to ~2200 °C at 100 mJ·cm^{-2} and ~3500 °C at 300 mJ·cm^{-2}. To understand the temperature rise at different depths in $SrTiO_3$, thermal profiles are further analyzed at different laser energy densities, as a result of which the plot for 300 mJ·cm^{-2} is shown in Figure 1b. The results illustrate that melting in $SrTiO_3$ occurs within ~100 nm skin-depth. While the temperature increase still takes place below this depth from the surface, no melting is observed. Based on these simulations, a laser energy density of 300 mJ·cm^{-2} is determined to be sufficient for $SrTiO_3$ surface modification through melting and recrystallization and is used for the irradiation experiments and subsequent studies of the atomic-scale structural transformations.

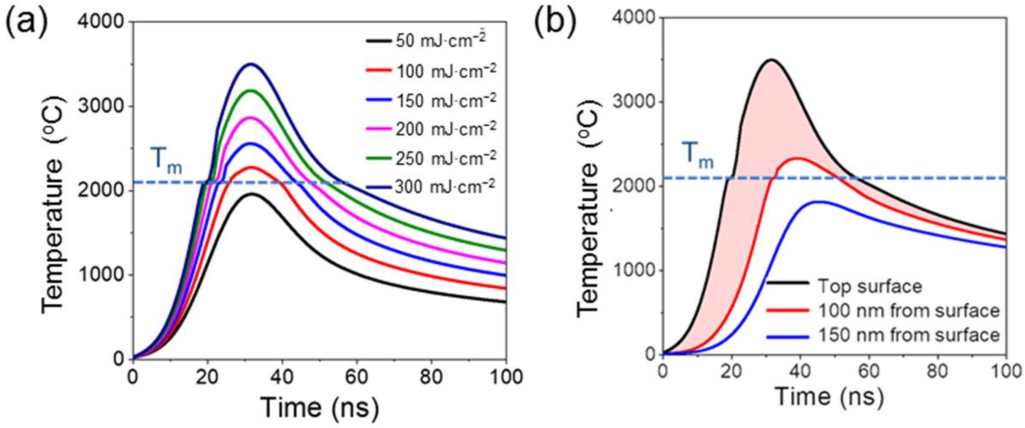

Figure 1. Numerical analysis of nanosecond pulsed laser irradiated $SrTiO_3$: (**a**) temperature vs. time profiles at various laser energy densities, (**b**) temperature vs. time profiles with the change of depth for a laser energy density of 300 mJ·cm^{-2}.

Figure 2a presents a representative overview ADF image from the [100] crystallographic direction of a single crystal $SrTiO_3$, irradiated normally with the laser energy density of 300 mJ·cm^{-2}. The total thickness of the irradiation-affected region appears to be ~100 ± 5 nm from the surface, which is consistent with the predictions from thermal profile simulations suggesting this region underwent recrystallization and possible phase transformation. Below this region, pristine/undamaged $SrTiO_3$ is present with an ordered lattice structure consisting of a uniform contrast in the ADF image. The cross-sectional image reveals the formation of two regions: (i) amorphous and (ii) disordered crystalline as a result of laser irradiation on the surface of single-crystalline $SrTiO_3$. The region with a depth of ~35 nm on the top surface shows an amorphous structure that was transformed from crystalline $SrTiO_3$. The presence of a ~65 nm thick layer of disordered/damaged crystalline $SrTiO_3$ can be seen below the amorphous layer based on a distinct contrast that emerged in the ADF images due to strain contrast. The evolution of this contrast is possibly related to the defect formation and chemical inhomogeneity in $SrTiO_3$. A schematic atomic model of ideal $SrTiO_3$ is depicted in Figure 2b, showing the Sr and Ti atoms superimposed on the ADF image. The model illustrates an ordered structure that allows an understanding of the crystal lattice positions of Sr and Ti atoms.

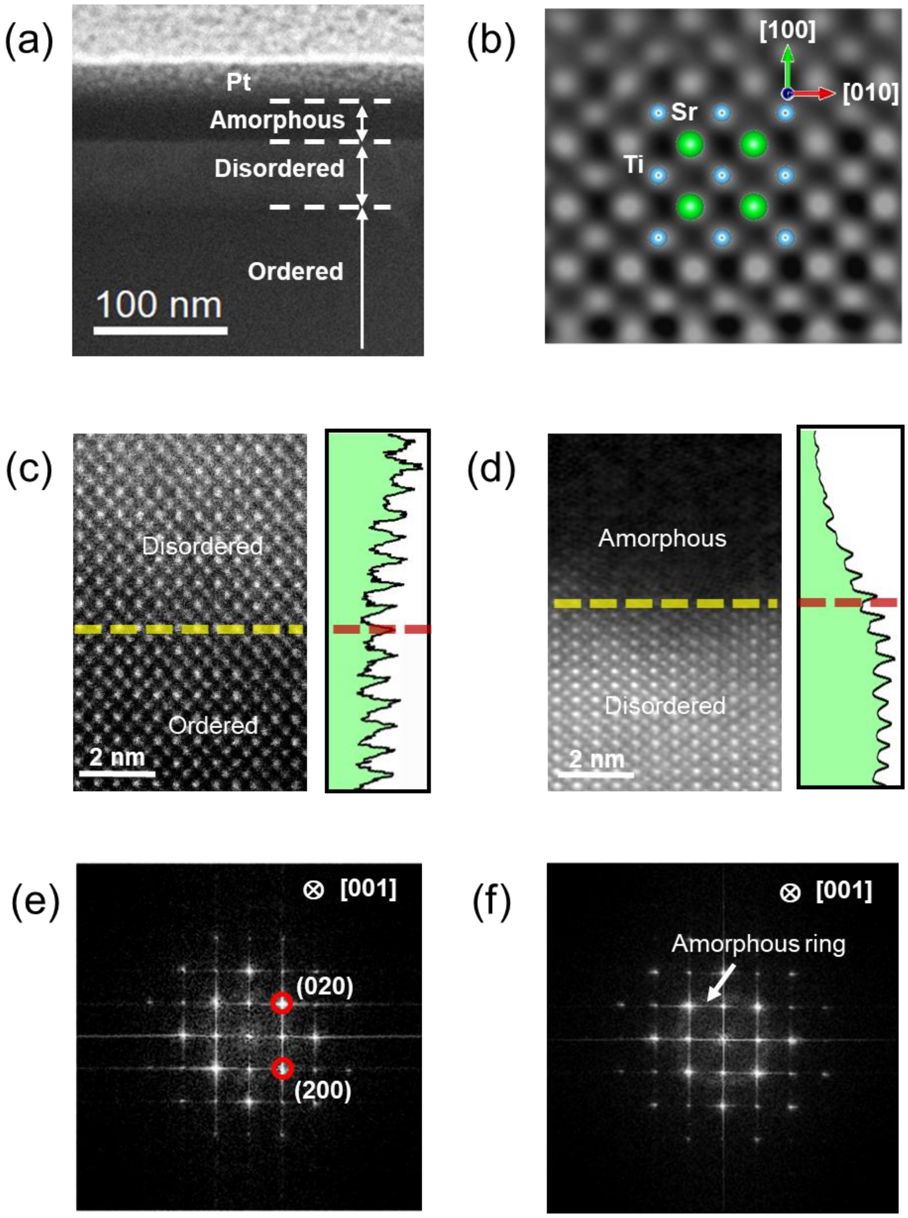

Figure 2. (**a**) The cross-sectional STEM image showing amorphous, disordered, and ordered regions. (**b**) Schematic model of $SrTiO_3$ in [001] zone axis superimposed over the ordered lattice structure. (**c**) ADF image depicting disordered and ordered region, the plot adjacent illustrates an intensity profile. Similarly, (**d**) shows an ADF image depicting disordered and amorphous regions, the plot adjacent illustrates the intensity profile. (**e**,**f**) Depicts fast Fourier transforms from ordered/disordered region and disordered/amorphous region, respectively.

Figure 2c shows an atomic resolution ADF image of regions containing disordered/ordered regions. These regions are distinguished based on the difference in the contrast that is more prominent in the disordered region where the intensity is more sensitive to the strain fields evolving from irradiation-induced defect formation [18,37], whereas the contrast in the ordered $SrTiO_3$ lattice is primarily dominated by z-contrast.

The plot adjacent to it depicts an intensity profile from a disordered/ordered region. The enhancement in the background intensity of the disordered region corresponds to the strain fields in the disordered region. Figure 2d shows an ADF image from the top region consisting of the disordered region interfacing with amorphous $SrTiO_3$. The disordered region could be identified by atomic columns, while in the amorphous region we see a featureless contrast due to the randomly oriented atoms. The intensity profile as shown in the adjacent figure shows an enhancement in the background intensity due to disordering in the lattice structure.

Fast Fourier transforms (FFTs) from disordered/ordered and disordered/amorphous regions are shown in Figure 2e,f, respectively. FFTs reveal diffraction spots and a halo-ring pattern corresponding to crystalline and amorphous regions, respectively. These obtained FFTs are quantified using a standard cubic $SrTiO_3$ phase, having the space group of $pm\bar{3}m$ [38,39]. The lattice parameters of cubic $SrTiO_3$ (a = b = c = 3.945 Å) are used for identifying inter-planer spacing. The atomic resolution ADF images (as shown in Figure 2c,d) show distinct interfaces between the three regions and a first-order transformation between the ordered and amorphous phase during the recrystallization process.

Figure 3a illustrates an ADF image with an overlaid pixilated ADF image from a region of interest (ROI) consisting of ordered, disordered, and amorphous regions. The pixilated ADF is obtained simultaneously with STEM-EELS from the ROI showing the size of each pixel over which EELS data are acquired while showing the ADF image intensity. The atomic-scale structural transformation consists of highly non-equilibrium melting and cooling events within a nanosecond time scale, and therefore EELS elemental map provides a comparative study of the elemental distribution. The EELS maps for Ti and O are as shown in Figure 3b,c, respectively. Each pixel in the EELS map is directly related to the energy registered at the detector as counts [40]. The Ti-EELS map remains mostly unchanged, revealing the presence of Ti throughout the ROI. However, the O intensity map shows a gradual decrease in Figure 3c. This could be due to the disruption of the atomic column channels in the disordered and amorphous regions, as well as the formation of oxygen vacancies which lower the overall intensity of the EELS profile of the O-K edge. The interfaces between ordered/disordered and disordered/amorphous regions are distinguishable from the O-EELS map, also shown in Figure 3c by a dotted line. It is well-recognized that during non-equilibrium melting and recrystallization process, the lattice disordering is seen leading to the formation of oxygen vacant sites. To understand the consequences of laser irradiation on the atomic structure of various regions of $SrTiO_3$, a detailed analysis of the fine structures of Ti– $L_{2,3}$ and O-K edges is carried out in the subsequent sections.

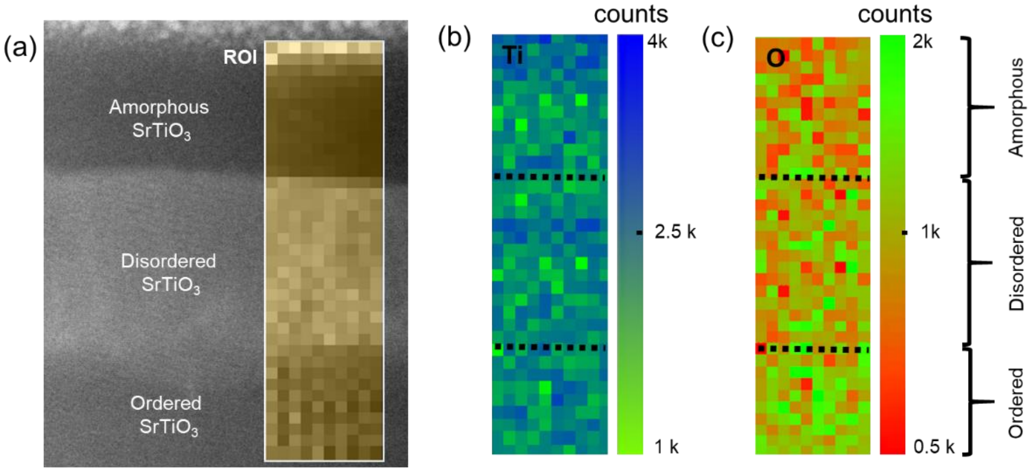

Figure 3. (**a**) Shows an ADF image with an overlaid region of interest (ROI) taken simultaneously to obtain an EELS map. (**b**,**c**) Corresponding EELS color maps for Ti and O are obtained over the ordered-amorphous regions.

Figure 4 shows the spatially resolved energy-loss near-edge structure (ELNES) for the Ti– $L_{2,3}$ edge, and O-K edge from the ordered, disordered, and amorphous regions, respectively. Particularly, these edges result from spin-orbit split, i.e., for Ti $2p_{3/2}$, $2p_{1/2}$ to 3d, and O 1s to 2p transitions, respectively, and are of critical importance for studying cation coordination and defect chemistry [41,42]. An energy-loss near-edge structure of Ti– $L_{2,3}$ edge for the ordered $SrTiO_3$ is shown in Figure 4a, which demonstrates the presence of two peaks in both the L_3 and L_2, and thus a total of four distinct peaks in the Ti–$L_{2,3}$ edge. The presence of these peaks in the Ti–$L_{2,3}$ edge occurs due to a crystal field splitting in the ordered $SrTiO_3$ which is well-established. The splitting of L_3– edge referred to as L_3– t_{2g} and L_3– e_g occurs at 459.3 eV and 461.5 eV, respectively, while the splitting of L_2–edge referred to as L_2– t_{2g} and L_2–e_g occurs at 464.5 eV and 466.8 eV, respectively. To examine the changes occurring in the ELNES spectra among ordered, disordered, and amorphous regions, a Gaussian peak fitting routine is performed, as shown in Figure 4. This also helps in understanding the details of EELS' fine structure by subtracting the quantum mechanical noise from the ELNES coming from the detector. With the experimentally acquired spectra of the Ti– $L_{2,3}$ edge and the fitted Gaussian peaks shown in Figure 4a–c, it is observed that the crystal field splitting exists in all ordered, disordered, and amorphous regions. The observation of crystal field splitting in the disordered and amorphous regions indicates the presence of short-range ordering of Ti-O bonds in spite of the increase in the lattice distortions and rearrangement under laser irradiation. The evidence of short-range ordering of Ti-O bonds in the amorphous region is consistent with the results reported in the pyrochlore structured complex metal titanate system of $Gd_2Ti_2O_7$ [42,43] where atomic disordering occurred via energetic ion-irradiation. In an important observation, we note that the e_g peak merges with the t_{2g} peak in the disordered structure, and this is even more pronounced in the amorphous structure. This merging of peaks suggests an overlapping and broadening of energy bands due to structural disordering [41].

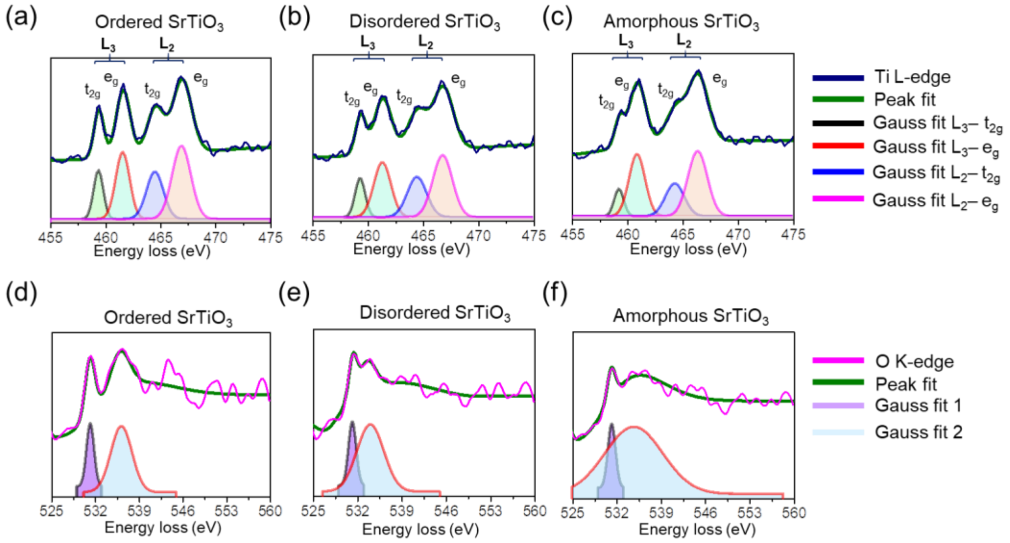

Figure 4. (**a**–**c**) Shows the ELNES for Ti– $L_{2,3}$ edge from ordered, disordered, and amorphous region, respectively. Whereas (**d**–**f**) depicts the ELNES for the O-K edge from ordered, disordered, and amorphous regions, respectively.

Figure 4d–f show ELNES from the O-K edge corresponding to ordered, disordered, and amorphous regions, respectively. To gain further insights into the changes in the O-K edge, ELNES spectra are deconvoluted by fitting Gaussian peaks. The O-K edge is sensitive to the changes in the local electronic structures and transformations [44]. We observe characteristic changes in the pre-peak as the transition occurs from the ordered to amorphous structure while the position of the O K-edge remains largely unchanged. A careful examination of the pre-peaks reveals that the pre-peaks corresponding to the ordered phase are quite distinct and merge with the main O-K peak in the disordered as well as in the amorphous phase. This finding supports the earlier discussed result from Ti–L_{32} ELNES that there is an overlapping of energy bands due to structural disordering in the disordered and amorphous phase.

These changes in the ELNES observed in the Ti– $L_{2,3}$ edge and O-K edge from the ordered, disordered, and amorphous regions, respectively, are the fingerprints of the variation of the Ti local environment. These may occur due to (i) a change in Ti– O coordination number or (ii) distortion of Ti– O polyhedra. This can be understood through a careful analysis of the fine structure of Ti– $L_{2,3}$ edge in the three regions, as shown in Figure 5.

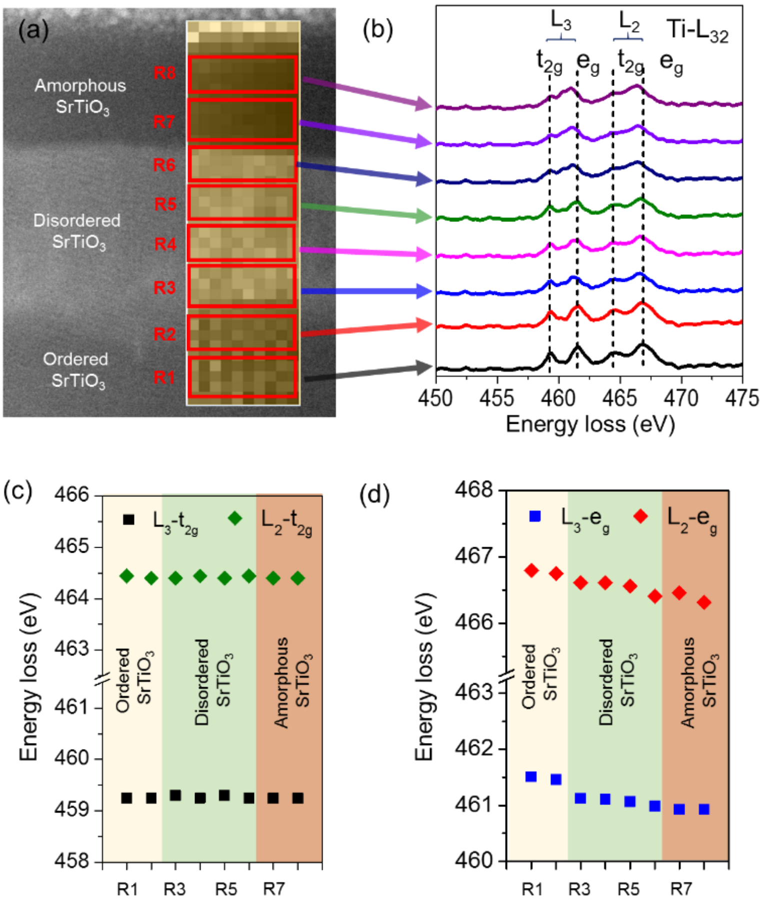

Figure 5. (**a**) Depicts an ADF image overlaid with a pixelated ADF image (inset reveals R1 to R8 regions for the collection of EELS spectra), (**b**) shows Ti–$L_{2,3}$ edge character from the region R1 to R8. (**c**) Plots showing the energy position of fitted peaks for Ti– t_{2g} peaks corresponding to regions R1 to R8. Similarly, (**d**) illustrates the energy position of fitted peaks for Ti– e_g peaks corresponding to regions R1 to R8, within the fitting deviation limits.

Figure 5a shows an ADF image overlaid with a pixelated ADF image acquired with EELS over an ROI. To conduct a detailed fine structure analysis, the overall ROI is divided into R1–R8 regions, where R1–2, R3–6, and R7–8 belong to ordered, disordered, and amorphous regions, respectively, as shown in Figure 5a. The corresponding ELNES for Ti–$L_{2,3}$ edges collected from these regions are displayed in Figure 5b. From ordered to amorphous regions, we observe a variation in the ELNES characteristics of Ti–$L_{2,3}$ edges. The Ti–$L_{2,3}$ edge from the region R1 and R2 shows four distinct peaks, i.e., L_3– t_{2g}, e_g, L_2– t_{2g}, and e_g, corresponding to ordered Ti-O octahedra in $SrTiO_3$. Observing the disordered structure i.e., Ti–$L_{2,3}$ edges from R3–R6, we note a broadening of t_{2g} and e_g peaks which continues to further broaden in the amorphous region. This broadening is attributed to the loss in the crystallinity or long-range ordering in the crystal structure. This eventually progresses into the amorphous region.

Closely observing the Ti–$L_{2,3}$ edges from the regions R1–R8, it is observed that the Ti– e_g peaks are more sensitive to the changes in the crystal structure. To gain insights into this behavior, Ti– t_{2g} and Ti– e_g energy positions are plotted with the regions corresponding to R1–R8. These plots are illustrated in Figure 5c,d, respectively. It is evident from Figure 5c that the energy positions of the Ti– t_{2g} remain unchanged for each of the phases, i.e., ordered to amorphous. On the other hand, the most prominent change in the Ti– e_g energy positions occurs between R2 and R3, which correspond to ordered and disordered phases. It can be seen that the energy peak positions of Ti– e_g decrease to a lower value in the disordered and amorphous regions, as shown in Figure 5d. However, the energy positions in these disordered regions show little change as compared to that in the ordered regions, in spite of the contrasting degree of disordering.

Based on the ELNES data presented in Figure 5, a quantitative change in the oxidation state of Ti in the three regions is determined. Figure 6 shows the variation of the transformation of Ti^{+4} from the ordered $SrTiO_3$ structure to a mixture of +4 and +3 oxidation states in the disordered regions. In an ordered $SrTiO_3$ structure corresponding to region R1, four peaks, i.e., L_3– t_{2g}, e_g, L_2– t_{2g}, and e_g, are observed for Ti^{+4} oxidation state. For reference, EELS spectra from powdered Ti_2O_3 of the Ti^{+3} oxidation state are analyzed, which were obtained from a previously reported study [45]. The integrated intensity was calculated using a Gaussian peak fitting routine. We observe a reduction in the intensity of the Ti–$L_{2,3}$ edge as the peak broadens and t_{2g} merges with e_g as we move from the Ti^{+4} oxidation state to the Ti^{+3} oxidation state. This was used as a parameter to understand the percentage of transformation in the subsequent regions, i.e., from the ordered to amorphous region. In the disordered region, the maximum transformation of Ti^{+4} is observed as 16.2 ± 0.2%, whereas in the amorphous region, the maximum transformation is observed as 20.2 ± 0.2%.

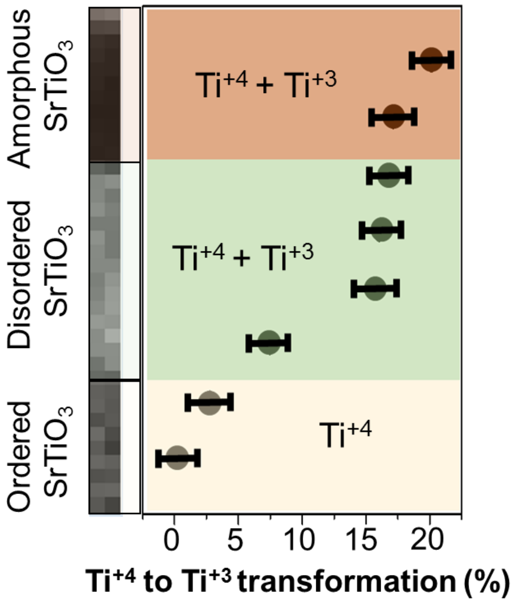

Figure 6. Depicts a variation of Ti oxidation states i.e., from ordered structure to amorphous region.

In an ordered $SrTiO_3$ structure, Ti^{+4} ions have six-fold symmetry coordinated by O^{2-} ions, where the Ti cation is at the center of the octahedron. This creates equivalent Ti-O bonds, leading to further Sr^{+2} ions surrounded by four TiO_6 octahedra [39]. $SrTiO_3$ is a good insulator with a bandgap of 3.2 eV (at T = 0 K) [21] and a possible candidate for high dielectric material, replacing SiO_2 [46]. Due to the pulsed laser irradiation, oxygen migration quickens in the $SrTiO_3$ structure. This leads to the formation of vacancies exceeding the equilibrium state. Therefore, in localized regions, the Ti^{+4} oxidation state transforms into a Ti^{+3} oxidation state. In our case, we observe a higher degree of disorder that can be correlated to the presence of a large number of non-equilibrium vacancies. Hence, we observe a greater transformation of the Ti^{+4} oxidation state to Ti^{+3} oxidation state in the amorphous region, resulting in the formation of an oxygen deficit $SrTiO_{3-\delta}$ structure. We conclude that the presence of structural defects such as vacancies leads to the variation in electrical properties [47]. This transformation behavior in the $SrTiO_3$ crystal structure leads to localized polarization. This polarization effect could lead to future applications as a promising electronic material.

4. Conclusions

In this research, the thermal transport simulations predict the melting of the $SrTiO_3$ surface by laser irradiation with the laser energy density of 300 mJ·cm^{-2} and above. This phenomenon results in the transformation of the crystalline $SrTiO_3$ into disordered and amorphous phases. Atomic-resolution electron microscopy was utilized to understand atomic rearrangements and structural transformations in $SrTiO_3$ single crystal irradiated from the [001] crystallographic direction. Due to nanosecond pulsed laser irradiation-induced melting and ultrafast quenching, the ordered single-crystalline $SrTiO_3$ transforms into an amorphous phase with an interposing disordered crystalline region between amorphous and ordered phase. The amorphous region was measured as ~35 nm, and the disordered region was ~65 nm in thickness. With EELS analysis, we confirmed the transformation of Ti^{+4} to Ti^{+3} due to oxygen vacancy formation. In the disordered region, the maximum transformation of Ti^{+4} was observed as $16.2 \pm 0.2\%$, whereas in the amorphous region, the maximum transformation was observed as $20.2 \pm 0.2\%$. We finally deduce that, while the degree of the disorder increases from atomically disordered to amorphous transition in $SrTiO_3$ under laser-irradiation, the transformation of Ti^{+4} to Ti^{+3} initiates to form an oxygen deficit $SrTiO_{3-\delta}$ structure. This study enables the identification of the interplay of laser irradiation and correlated transformation of Ti^{+4} to Ti^{+3} to functionalize pristine $SrTiO_3$ for potential electronic, optical, and magnetic applications.

Author Contributions: Conceptualization, R.S.; methodology, A.K.G., S.G., S.M. and R.S.; software, A.K.G., S.M. and R.S.; validation, R.S.; writing—original draft preparation, A.K.G. and S.M.; writing—review and editing, A.K.G., S.M. and R.S.; supervision, R.S. All authors have read and agreed to the published version of the manuscript.

Funding: R.S. acknowledges the support of faculty start-up funding at Oklahoma State University.

Institutional Review Board Statement: Not applicable.

Informed Consent Statement: Not applicable.

Data Availability Statement: Not applicable.

Acknowledgments: The electron microscopic data acquisition in this research was conducted at the Center for Nanophase Materials Sciences at ORNL, which is a DOE Office of Science User Facility.

Conflicts of Interest: The authors declare no conflict of interest.

References

1. Rao, S.S.; Lee, Y.F.; Prater, J.T.; Smirnov, A.I.; Narayan, J. Laser annealing induced ferromagnetism in $SrTiO_3$ single crystal. *Appl. Phys. Lett.* **2014**, *105*, 042403. [CrossRef]
2. Chan, N.H.; Sharma, R.K.; Smyth, D.M. Nonstoichiometry in $SrTiO_3$. *J. Electrochem. Soc.* **1981**, *128*, 1762. [CrossRef]
3. Gerblinger, J.; Meixner, H. Fast oxygen sensors based on sputtered strontium titanate. *Sens. Actuators B Chem.* **1991**, *4*, 99–102. [CrossRef]
4. Weber, W.J.; Zarkadoula, E.; Pakarinen, O.H.; Sachan, R.; Chisholm, M.F.; Liu, P.; Xue, H.; Jin, K.; Zhang, Y. Synergy of elastic and inelastic energy loss on ion track formation in $SrTiO_3$. *Sci. Rep.* **2015**, *5*, 7726. [CrossRef] [PubMed]
5. Xue, H.; Zarkadoula, E.; Sachan, R.; Zhang, Y.; Trautmann, C.; Weber, W.J. Synergistically-enhanced ion track formation in pre-damaged strontium titanate by energetic heavy ions. *Acta Mater.* **2018**, *150*, 351–359. [CrossRef]
6. Toulemonde, M.; Weber, W.J.; Li, G.; Shutthanandan, V.; Kluth, P.; Yang, T.; Wang, Y.; Zhang, Y. Synergy of nuclear and electronic energy losses in ion-irradiation processes: The case of vitreous silicon dioxide. *Phys. Rev. B* **2011**, *83*, 054106. [CrossRef]

7. Thomé, L.; Debelle, A.; Garrido, F.; Trocellier, P.; Serruys, Y.; Velisa, G.; Miro, S. Combined effects of nuclear and electronic energy losses in solids irradiated with a dual-ion beam. *Appl. Phys. Lett.* **2013**, *102*, 141906. [CrossRef]
8. Sall, M.; Monnet, I.; Grygiel, C.; d'Etat, B.B.; Lebius, H.; Leclerc, S.; Balanzat, E. Synergy between electronic and nuclear energy losses for color center creation in AlN. *EPL (Europhys. Lett.)* **2013**, *102*, 26002. [CrossRef]
9. Zhang, Y.; Aidhy, D.S.; Varga, T.; Moll, S.; Edmondson, P.D.; Namavar, F.; Jin, K.; Ostrouchov, C.N.; Weber, W.J. The Effect of Electronic Energy Loss on Irradiation-Induced Grain Growth in Nanocrystalline Oxides. *Phys. Chem. Chem. Phys.* **2014**, *16*, 8051–8059. [CrossRef]
10. Wang, Y.Y.; Grygiel, C.; Dufour, C.; Sun, J.R.; Wang, Z.G.; Zhao, Y.T.; Xiao, G.Q.; Cheng, R.; Zhou, X.M.; Ren, J.R.; et al. Energy Deposition by Heavy Ions: Additivity of Kinetic and Potential Energy Contributions in Hillock Formation on CaF_2. *Sci. Rep.* **2014**, *4*, 5742. [CrossRef]
11. Debelle, A.; Backman, M.; Thomé, L.; Weber, W.J.; Toulemonde, M.; Mylonas, S.; Boulle, A.; Pakarinen, O.H.; Juslin, N.; Djurabekova, F.; et al. Combined Experimental and Computational Study of the Recrystallization Process Induced by Electronic Interactions of Swift Heavy Ions with Silicon Carbide Crystals. *Phys. Rev. B* **2012**, *86*, 100102. [CrossRef]
12. Weber, W.J.; Zhang, Y.; Xiao, H.; Wang, L. Dynamic Recovery in Silicate-Apatite Structures under Irradiation and Implications for Long-Term Immobilization of Actinides. *RSC Adv.* **2012**, *2*, 595–604. [CrossRef]
13. Pervolaraki, M.; Mihailescu, C.N.; Luculescu, C.R.; Ionescu, P.; Dracea, M.D.; Pantelica, D.; Giapintzakis, J. Picosecond Ultrafast Pulsed Laser Deposition of $SrTiO_3$. *Appl. Surf. Sci.* **2015**, *336*, 278–282. [CrossRef]
14. Sachan, R.; Chisholm, M.F.; Ou, X.; Zhang, Y.; Weber, W.J. Energetic Ion Irradiation-Induced Disordered Nanochannels for Fast Ion Conduction. *JOM* **2019**, *71*, 103–108. [CrossRef]
15. Leino, A.A.; Samolyuk, G.D.; Sachan, R.; Granberg, F.; Weber, W.J.; Bei, H.; Liu, J.; Zhai, P.; Zhang, Y. GeV Ion Irradiation of NiFe and NiCo: Insights from MD Simulations and Experiments. *Acta Mater.* **2018**, *151*, 191–200. [CrossRef]
16. Sachan, R.; Pakarinen, O.H.; Liu, P.; Patel, M.K.; Chisholm, M.F.; Zhang, Y.; Wang, X.L.; Weber, W.J. Structure and Band Gap Determination of Irradiation-Induced Amorphous Nano-Channels in $LiNbO_3$. *J. Appl. Phys.* **2015**, *117*, 135902. [CrossRef]
17. Gupta, A.K.; Arora, G.; Aidhy, D.S.; Sachan, R. $\sum 3$ Twin Boundaries in $Gd_2Ti_2O_7$ Pyrochlore: Pathways for Oxygen Migration. *ACS Appl. Mater. Interfaces* **2020**, *12*, 45558–45563. [CrossRef]
18. Kan, D.; Terashima, T.; Kanda, R.; Masuno, A.; Tanaka, K.; Chu, S.; Kan, H.; Ishizumi, A.; Kanemitsu, Y.; Shimakawa, Y.; et al. Blue-Light Emission at Room Temperature from Ar+ -Irradiated $SrTiO_3$. *Nat. Mater.* **2005**, *4*, 816–819. [CrossRef]
19. Nova, T.F.; Disa, A.S.; Fechner, M.; Cavalleri, A. Metastable Ferroelectricity in Optically Strained $SrTiO_3$. *Science* **2019**, *364*, 1075–1079. [CrossRef]
20. Hanzig, J.; Abendroth, B.; Hanzig, F.; Stöcker, H.; Strohmeyer, R.; Meyer, D.C.; Lindner, S.; Grobosch, M.; Knupfer, M.; Himcinschi, C.; et al. Single Crystal Strontium Titanate Surface and Bulk Modifications Due to Vacuum Annealing Vacuum Annealing. *J. Appl. Phys.* **2011**, *110*, 064107. [CrossRef]
21. Hill, N.A. Density Functional Studies of Multiferroic Magnetoelectrics. *Annu. Rev. Mater. Sci.* **2002**, *32*, 1–37. [CrossRef]
22. Choi, H.J.; Park, S.W.; Han, G.D.; Na, J.; Kim, G.; Shim, J.H. Resistive Switching Characteristics of Polycrystalline $SrTiO_3$ Films. *Appl. Phys. Lett.* **2014**, *104*, 242105. [CrossRef]
23. Spurgeon, S.R.; Kaspar, T.C.; Shutthanandan, V.; Gigax, J.; Shao, L.; Sassi, M. Asymmetric Lattice Disorder Induced at Oxide Interfaces. *Adv. Mater. Interfaces* **2020**, *7*, 1901944. [CrossRef]
24. Crespillo, M.L.; Graham, J.T.; Agulló-López, F.; Zhang, Y.; Weber, W.J. Role of Oxygen Vacancies on Light Emission Mechanisms in $SrTiO_3$ Induced by High-Energy Particles. *J. Phys. D Appl. Phys.* **2017**, *50*, 155303. [CrossRef]
25. Brovko, O.O.; Tosatti, E. Controlling the Magnetism of Oxygen Surface Vacancies in $SrTiO_3$ through Charging. *Phys. Rev. Mater.* **2017**, *1*, 044405. [CrossRef]
26. Cha, S.H.; Han, Y.H. Effects of Oxygen Vacancies on Relaxation Behavior of Mg-Doped $BaTiO_3$. *Jpn. J. Appl. Phys.* **2006**, *45*, 7797. [CrossRef]
27. Lu, W.; Song, W.; Yang, P.; Ding, J.; Chow, G.M.; Chen, J. Strain Engineering of Octahedral Rotations and Physical Properties of $SrRuO_3$ Films. *Sci. Rep.* **2015**, *5*, 10245. [CrossRef]
28. Frenkel, A.I.; Ehre, D.; Lyahovitskaya, V.; Kanner, L.; Wachtel, E.; Lubomirsky, I. Origin of Polarity in Amorphous $SrTiO_3$. *Phys. Rev. Lett.* **2007**, *99*, 215502. [CrossRef]
29. Joshi, P.C.; Krupanidhi, S.B. Structural and electrical characteristics of $SrTiO_3$ thin films for dynamic random access memory applications. *J. Appl. Phys.* **1993**, *73*, 7627–7634. [CrossRef]
30. Lu, S.G.; Zhu, X.H.; Mak, C.L.; Wong, K.H.; Chan, H.L.W.; Choy, C.L. High tunability in compositionally graded epitaxial barium strontium titanate thin films by pulsed-laser deposition. *Appl. Phys. Lett.* **2003**, *82*, 2877–2879. [CrossRef]
31. Shenoy, U.S.; Bantawal, H.; Bhat, D.K. Band Engineering of $SrTiO_3$: Effect of Synthetic Technique and Site Occupancy of Doped Rhodium. *J. Phys. Chem. C* **2018**, *122*, 27567–27574. [CrossRef]
32. Domen, K.; Kudo, A.; Onishi, T. Mechanism of photocatalytic decomposition of water into H_2 and O_2 over NiO $SrTiO_3$. *J. Catal.* **1986**, *102*, 92–98. [CrossRef]
33. Hui, S.; Petric, A. Evaluation of Yttrium-Doped $SrTiO_3$ as an Anode for Solid Oxide Fuel Cells. *J. Eur. Ceram. Soc.* **2002**, *22*, 1673–1681. [CrossRef]
34. Verbraeken, M.C.; Ramos, T.; Agersted, K.; Ma, Q.; Savaniu, C.D.; Sudireddy, B.R.; Irvine, J.T.S.; Holtappels, P.; Tietz, F. Modified Strontium Titanates: From Defect Chemistry to SOFC Anodes. *RSC Adv.* **2015**, *5*, 1168–1180. [CrossRef]

35. Ihrig, H.; Hengst, J.H.T.; Klerk, M. Conductivity-dependent cathodoluminescence in $BaTiO_3$, $SrTiO_3$ and TiO_2. *Z. Für Phys. B Condens. Matter* **1981**, *40*, 301–306. [CrossRef]
36. Lehuta, K. Dopant-Defect Engineering in Strontium Titanate-Based Materials. Ph.D. Thesis, University of Massachusetts, Amherst, MA, USA, 2017.
37. Gupta, S.; Sachan, R.; Narayan, J. Scale-up of Q-carbon and Nanodiamonds by Pulsed Laser Annealing. *Diam. Relat. Mater.* **2019**, *99*, 107531. [CrossRef]
38. Persson, K. *Materials Data on $SrTiO_3$ (SG:221) by Materials Project*; OSTI: Oak Ridge, TN, USA, 2014. [CrossRef]
39. Gupta, A.K.; Gupta, S.; Sachan, R. Laser Irradiation Induced Atomic Structure Modifications in Strontium Titanate. *JOM* **2022**, *74*, 143–150. [CrossRef]
40. Plotkin-swing, B.; Corbin, G.J.; De Carlo, S.; Dellby, N.; Hoermann, C.; Hoffman, M.V.; Lovejoy, T.C.; Meyer, C.E.; Mittelberger, A.; Pantelic, R.; et al. Hybrid Pixel Direct Detector for Electron Energy Loss Spectroscopy. *Ultramicroscopy* **2020**, *217*, 113067. [CrossRef]
41. Sachan, R.; Cooper, V.R.; Liu, B.; Aidhy, D.S.; Voas, B.K.; Lang, M.; Ou, X.; Trautmann, C.; Zhang, Y.; Chisholm, M.F.; et al. Forging Fast Ion Conducting Nanochannels with Swift Heavy Ions: The Correlated Role of Local Electronic and Atomic Structure. *J. Phys. Chem. C* **2017**, *121*, 975–981. [CrossRef]
42. Sachan, R.; Zhang, Y.; Ou, X.; Trautmann, C.; Chisholm, M.F.; Weber, W.J. New Insights on Ion Track Morphology in Pyrochlores by Aberration Corrected Scanning Transmission Electron Microscopy. *J. Mater. Res.* **2016**, *32*, 928–935. [CrossRef]
43. Aidhy, D.S.; Sachan, R.; Zarkadoula, E.; Pakarinen, O.; Chisholm, M.F.; Zhang, Y.; Weber, W.J. Fast Ion Conductivity in Strained Defect-Fluorite Structure Created by Ion Tracks in $Gd_2Ti_2O_7$. *Sci. Rep.* **2015**, *5*, 16297. [CrossRef] [PubMed]
44. Mandal, S.; Gupta, A.K.; Beavers, B.H.; Singh, V.; Narayan, J.; Sachan, R. Atomic-Scale Insights on Large-Misfit Heterointerfaces in LSMO/MgO/c-Al_2O_3. *Crystals* **2021**, *11*, 1493. [CrossRef]
45. Li, Y.; Wang, Q.; An, M.; Li, K.; Wehbe, N.; Zhang, Q.; Dong, S.; Wu, T. Nanoscale Chemical and Valence Evolution at the Metal/Oxide Interface: A Case Study of Ti/$SrTiO_3$. *Adv. Mater. Interfaces* **2016**, *3*, 1600201. [CrossRef]
46. Dai, S.; Lu, H.; Chen, F.; Chen, Z.; Ren, Z.Y.; Ng, D.H.L. In-Doped $SrTiO_3$ Ceramic Thin Films. *Appl. Phys. Lett.* **2002**, *80*, 3545–3547. [CrossRef]
47. Akhtar, M.J.; Akhtar, Z.U.N.; Jackson, R.A.; Catlow, C.R.A. Computer Simulation Studies of Strontium Titanate. *J. Am. Ceram. Soc.* **1995**, *78*, 421–428. [CrossRef]